Search for heavy resonances decaying into a W boson and a Higgs boson in final states with leptons and b-jets in $139\,\text{fb}^{-1}$ of pp collisions at $\sqrt{s} = 13\,\text{TeV}$ with the ATLAS detector

The ATLAS Collaboration

This note presents a search for a new resonance W' decaying into a W boson and a 125 GeV Higgs boson H in the $\ell^\pm \nu b \bar{b}$ final state, where $\ell = e$ or μ, using pp collision data at 13 TeV corresponding to an integrated luminosity of 139 fb^{-1} collected by the ATLAS detector at the LHC. The search is conducted by examining the reconstructed invariant mass distributions of $W' \to WH$ candidates in the mass range from 400 GeV to 5 TeV. No significant excess is observed and 95% confidence level upper limits between 1.3 pb and 0.56 fb are placed on the production cross-section times branching fraction of W' bosons in Heavy-Vector-Triplet models.

1 Introduction

Following the discovery of the Higgs boson [1, 2], measurements of its properties so far indicate consistency with the Standard Model (SM) predictions. Nevertheless, several questions related to electroweak symmetry breaking remain open, in particular how the Higgs boson mass is protected against large radiative corrections (the naturalness problem [3–5]) and whether the Higgs boson is part of an extended scalar sector.

Various models with dynamical electroweak symmetry breaking scenarios attempt to solve the naturalness problem by assuming new strong interactions at a higher energy scale. These models generally predict the existence of new vector resonances that naturally decay into a vector boson and a Higgs boson, for example in Minimal Walking Technicolour [6–8], Little Higgs [9] or composite Higgs models [10, 11]. Resonance searches are typically not designed to be sensitive to all parameters of the underlying theory, thus generally simplified models are used, such as the Heavy Vector Triplet (HVT) parameterized Lagrangian [12, 13], which adds an additional $SU(2)_L$ field to the SM and provides a restricted number of new couplings.

This note presents a search for the production of new heavy vector bosons, denoted hereafter by W', that decay into a W boson and a SM Higgs boson H (m_H = 125.09 GeV), using the full Run-2 data set of proton-proton (pp) collisions collected by the ATLAS detector. The search targets leptonic decays of the W boson, $W \to \ell\nu$, where $\ell = e$ or μ, and requires b-quark pair decays for the Higgs boson, assuming the SM branching fractions: $\mathrm{BR}(H \to b\bar{b}/c\bar{c} = 0.5809/0.0029)$ [14].

Previous searches in similar final states have been performed using a partial Run-2 data set by CMS [15] and ATLAS [16–18]. Results have also been published in the fully-hadronic final states: ATLAS has performed a search [19] on the full Run-2 data set and CMS has published results [20] on partial data sets.

Apart from the significantly larger data set, several improvements have been implemented with respect to the previous publication [16], including improved b-tagging [21–24], lepton isolation [25, 26] and jet reconstruction [27–29] (see Sections 4 and 5).

The search is performed by making selections of signal regions (SRs) and of background-dominated control regions (CRs) based on requirements on kinematic properties of final-state particles and event-level quantities. At low transverse momenta, the two decay products of the Higgs boson are reconstructed as individual jets, while at high transverse momenta they are reconstructed as a single large-radius jet. The dominant backgrounds are modelled using Monte Carlo (MC) simulations, while the relatively small contribution from multijet events is estimated from control regions in the data. The other CRs are defined to improve the modelling of W+jets and top-quark backgrounds. The search presented in this note is performed by looking for a localised excess in the distribution of the reconstructed invariant mass m_{WH}.

The results from the W' search are interpreted in two HVT benchmark models. In the first model, referred to as *Model A*, the branching fractions to fermions and gauge bosons are comparable, as in some models with an extended gauge symmetry [30]. For *Model B*, fermionic couplings are suppressed, as in strong dynamical models such as the minimal composite Higgs model [31]. The search focuses on high resonance masses, from 400 GeV up to 5 TeV.

This note is structured as follows. Sections 2 and 3 provide a brief description of the ATLAS experiment, as well as the data and simulated samples. The event reconstruction and selections are discussed in Sections 4 and 5. The background estimation and systematic uncertainties are described in Sections 6 and 7. Finally, Section 8 provides the statistical analysis and a discussion of the results, while concluding remarks are given in Section 9.

2 ATLAS detector

The ATLAS detector [32] is a general-purpose particle detector used to investigate a broad range of physics processes. It includes an inner tracking detector (ID) surrounded by a thin superconducting solenoid, electromagnetic and hadronic calorimeters and a muon spectrometer (MS) incorporating three large superconducting toroid magnets with eight coils each. The ID consists of fine-granularity silicon pixel and microstrip detectors, and a straw-tube tracker. The silicon pixel detector includes an insertable B-Layer [33], which was installed before the start of Run-2. The ID is immersed in a 2 T axial magnetic field produced by the solenoid and provides precision tracking for charged particles in the range $|\eta| < 2.5$, where η is the pseudorapidity.[1] The straw-tube detector also provides transition radiation measurements for electron identification. The calorimeter system covers the pseudorapidity range $|\eta| < 4.9$. It is composed of sampling calorimeters with either liquid argon (LAr) or scintillator tiles as the active medium, and lead, steel, copper, or tungsten as the absorber material. The MS provides muon identification and momentum measurements for $|\eta| < 2.7$. The ATLAS detector has a two-level trigger system to select events for further analysis [34].

3 Data and Monte Carlo samples

The data used in this analysis were recorded with the ATLAS detector between 2015 and 2018 in pp-collisions at $\sqrt{s} = 13$ TeV and correspond to a total integrated luminosity of 139 fb^{-1} [35]. The data are required to satisfy criteria that ensure that the detector was in good operating condition. MC simulation samples are used to model background and signal processes.

Quark-antiquark annihilation induced production of W' bosons is generated with MADGRAPH5 2.3.3 [36] at leading-order (LO) accuracy in QCD interfaced with PYTHIA 8.186 [37], to model the parton shower (PS), hadronisation, and underlying event, using the A14 set of tuned parameters [38] and the NNPDF 2.3 LO parton density function (PDF) set [39]. Events are generated for a range of resonance masses from 400 GeV to 5 TeV using the benchmark HVT *Model A*. Separate generation of signal events for HVT *Model A* and *B* is not necessary as both give rise to a mass peak in the WH system with a width that is dominated by the experimental resolution. The Higgs boson decays into $b\bar{b}$ and $c\bar{c}$. Even though the search does not target the latter decay directly, it is sensitive to these types of events. However, the fraction of surviving $H \to c\bar{c}$ events in the signal regions is relatively low. The W bosons are required to decay semi-leptonically, $W \to \ell\nu$, with $\ell = e$ or μ.

The production of W and Z bosons in association with jets is simulated with the SHERPA 2.2.1 [40] generator using next-to-leading order (NLO) matrix elements (ME) for up to two partons, and LO matrix elements for up to four partons calculated with the COMIX [41] and OPENLOOPS [42–44] libraries. They are matched with the SHERPA parton shower [45] using the MEPS@NLO prescription [46–49] using the set of tuned parameters developed by the SHERPA authors. The NNPDF 3.0 NLO set of PDFs [50] is used and the samples are normalised to a next-to-next-to-leading order (NNLO) prediction [51].

---

[1] ATLAS uses a right-handed coordinate system with its origin at the nominal interaction point (IP) in the centre of the detector and the z-axis along the beam pipe. The x-axis points from the IP to the centre of the LHC ring, and the y-axis points upwards. Cylindrical coordinates (r, ϕ) are used in the transverse plane, ϕ being the azimuthal angle around the beam pipe. The pseudorapidity is defined in terms of the polar angle θ as $\eta = -\ln\tan(\theta/2)$. Angular distance is measured in units of $\Delta R \equiv \sqrt{(\Delta\eta)^2 + (\Delta\phi)^2}$.

The production of $t\bar{t}$ events is modelled using the PowhegBox 2 [52–55] generator at NLO with the NNPDF 3.0 NLO PDF set and the h_{damp} parameter[2] set to $1.5 \cdot m_{\mathrm{top}}$ [56], where $m_{\mathrm{top}} = 172.5$ GeV. The events are interfaced to Pythia 8.230 [57], using the A14 set of tuned parameters and the NNPDF 2.3 LO set of PDFs. The cross-section is calculated at NNLO accuracy including the resummation of next-to-next-to-leading logarithmic (NNLL) soft gluon terms with Top++2.0 [58–64].

The associated production of top quarks with W bosons (Wt), as well as s- and t-channel production of top quarks, are modelled using the PowhegBox 2 generator at approximately NNLO in QCD for the Wt and NLO in QCD for the s and t channels, using the five-flavour scheme and the NNPDF 3.0 NLO set of PDFs. The diagram removal scheme [65] is used to remove interference and overlap with $t\bar{t}$ production. The events are interfaced to Pythia 8.230 using the A14 set of tuned parameters and the NNPDF 2.3 LO set of PDFs.

Diboson events (WW, WZ, ZZ) are simulated using Sherpa 2.2.1 with the NNPDF 3.0 NNLO PDF set, including off-shell effects and Higgs-boson contributions, where appropriate. Diagrams with up to one additional emission are calculated with NLO precision in QCD, while diagrams with up to three parton emissions are described at LO accuracy [66]. They are merged and matched using the MEPS@NLO prescription. Loop-induced diboson processes that are initiated via the gg production mode are simulated at LO in QCD for diagrams with up to one additional parton emission at the matrix element using OpenLoops in Sherpa 2.2.2, using the NNPDF 3.0 NNLO PDF set.

Finally, the production of a Higgs boson in association with a vector boson is simulated using PowhegBox 2 [54] and interfaced with Pythia 8.212 for parton shower and non-perturbative effects. The Powheg prediction is at NLO accuracy in QCD for the VH boson plus one jet production. The loop-induced $gg \rightarrow ZH$ process is generated separately at LO. The PDF4LHC15 PDF set [67] and the AZNLO tune [68] of Pythia 8.212 are used. The $gg \rightarrow ZH$ production cross-section was calculated at NLO accuracy including the resummation of next-to-leading logarithmic (NLL) soft gluon terms [69].

A summary of event generators used for the simulation of signal and background processes is provided in Table 1.

Table 1: Summary of the Monte Carlo generators used to produce the various signal and background processes. The column "Perturbative accuracy of σ_{prod}" gives the precision in QCD of the inclusive production cross-section σ_{prod} applied to the respective process. The order at which the corresponding matrix elements are calculated in the Monte Carlo simulation is not necessarily the same as for the cross-section.

Process	Generator	Perturbative accuracy of σ_{prod}
$q\bar{q} \rightarrow W' \rightarrow WH \rightarrow lv + bb/cc$	MadGraph5 2.3.3 + Pythia 8	LO
$W \rightarrow \ell v, Z \rightarrow \ell\ell/vv$	Sherpa 2.2.1	NNLO
$t\bar{t}$	PowhegBox 2 + Pythia 8	NNLO+NNLL
single-top $s-$ and t-channels	PowhegBox 2 + Pythia 8	NLO
single-top Wt-channel	PowhegBox 2 + Pythia 8	approx. NNLO
$qg/q\bar{q} \rightarrow VV \rightarrow \ell\ell/\ell v/vv + q\bar{q}$	Sherpa 2.2.1	NLO
$gg \rightarrow VV \rightarrow \ell\ell/\ell v/vv + q\bar{q}$	Sherpa 2.2.2	NLO
$qg/q\bar{q} \rightarrow \ell\ell vv$	Sherpa 2.2.2	NLO
$qq \rightarrow WH \rightarrow \ell v + b\bar{b}$	PowhegBox 2 + Pythia 8	NNLO (QCD) and NLO (EW)
$qq \rightarrow ZH \rightarrow \ell\ell/vv + b\bar{b}$	PowhegBox 2 + Pythia 8	NNLO (QCD) and NLO (EW)
$gg \rightarrow ZH \rightarrow \ell\ell/vv + b\bar{b}$	PowhegBox 2 + Pythia 8	NLO+NLL

---

[2] The h_{damp} parameter is a resummation damping factor and one of the parameters that controls the matching of Powheg matrix elements to the parton shower and thus effectively regulates the high-p_{T} radiation against which the $t\bar{t}$ system recoils.

All simulated event samples include the effect of multiple pp interactions in the same and neighbouring bunch crossings (pile-up) by overlaying simulated minimum-bias events on each generated signal or background event. The minimum-bias events are simulated with the single-, double- and non-diffractive pp processes of PYTHIA 8.186 using the A3 tune [70] and the NNPDF 2.3 LO PDF set.

For all MADGRAPH and POWHEGBOX samples, the EVTGEN 1.6.0 program [71] is used for the bottom and charm hadron decays.

The generated samples are processed using the GEANT4-based ATLAS detector simulation [72, 73] and the same event reconstruction algorithms are used as for the data.

Simulated events are corrected to compensate for differences between data and simulations regarding the energy (or momentum) scale and resolution of leptons and jets, the efficiencies for the reconstruction, identification, isolation and triggering of leptons, as well as the tagging efficiency for heavy-flavour jets as detailed in Section 7.

4 Event reconstruction

Collision vertices are reconstructed from at least two ID tracks with transverse momentum $p_T > 500$ MeV [74]. Among all vertices, the one with the highest p_T^2 sum of all associated tracks is chosen to be the primary vertex (PV) of the event.

Three jet types are reconstructed, using the anti-k_t [75] algorithm implemented in the FASTJET package [76]. Small-radius (small-R) jets are reconstructed from noise-suppressed topological clusters in the calorimeter [77, 78] using a distance parameter of $R = 0.4$. They are required to have $p_T > 20$ GeV for central jets ($|\eta| < 2.5$) and $p_T > 30$ GeV for forward jets ($2.5 < |\eta| < 4.5$). To suppress central jets from pile-up interactions, they are required to pass the jet vertex tagger [79] selection if they are in the range $p_T < 120$ GeV and $|\eta| < 2.5$.

Large-radius (large-R) jets are used to reconstruct Higgs-boson candidates with high momenta for which the b-quarks are emitted close to each other. These jets are built using a distance parameter $R = 1.0$ and track-calorimeter clusters (TCCs) [29] as inputs. The TCCs are formed by combining information from the calorimeter and the ID. Trimming [80] is applied to remove the energy of clusters that originate from initial-state radiation, pile-up interactions or the underlying event. This is done by reclustering the constituents of the initial jet, using the k_t algorithm [81, 82], into smaller $R_{sub} = 0.2$ subjets and then removing any subjet that has a p_T less than 5% of the p_T of the parent jet [83]. The large-R jets are required to have $p_T > 250$ GeV and $|\eta| < 2.0$.

The momenta of both the large-R and small-R jets are corrected for energy losses in passive material and for the non-compensating response of the calorimeter. Small-R jets are also corrected for the average additional energy due to pile-up interactions [84, 85].

The third type of jets are clustered from ID tracks using a variable radius (VR), based on the anti-k_t algorithm, that shrinks with increasing p_T of the studied proto-jet [27]. VR track jets are used in this analysis for the identification of b-jets from decays of boosted Higgs bosons. They must contain at least two ID tracks compatible with the primary vertex and are required to have $|\eta| < 2.5$. In this analysis, only large-R jets with at least two ghost-associated [28] VR track jets with $p_T > 10$ GeV are retained.

Small-R jets and VR track jets containing b-hadrons are identified using the MV2c10 b-tagging algorithm [21–24], with an operating point that corresponds to a selection efficiency of 70% for b-jets, as measured in simulated $t\bar{t}$ events. Applying the b-tagging algorithm reduces the number of light-flavour and gluon jets, jets arising from hadronically decaying τ-leptons and c-quark jets by a factor of 300, 36 and 8.9, respectively [21]. To remove potential b-tagging performance issues in the selection of jets with an ambiguous association of tracks from heavy-flavour decays, events are removed if they contain an overlap between one of the VR track jets used for b-tagging and at least one VR track jet with a p_T above 5 GeV.

Electrons are reconstructed from ID tracks that are matched to clusters in the electromagnetic calorimeter and which come from the PV. The latter condition is satisfied by requirements on the transverse impact parameter significance, $|d_0|/\sigma(d_0) < 5.0$, and on the longitudinal impact parameter, $|z_0 \sin(\theta)| < 0.5$ mm. Electrons must satisfy requirements on the electromagnetic shower shape, track quality, and track–cluster matching, using a likelihood-based approach with a *Tight* working point (*LHTight*) [25]. They must also be isolated: both the calorimeter energy sum and the transverse momentum sum of all ID tracks within a variable-radius cone around the electron have to be smaller than 0.06 times the electron transverse energy (E_T). The maximum cone size is $\Delta R = 0.2$, shrinking for larger electron E_T.

Muons are reconstructed by matching tracks found in the ID to either full tracks or track segments reconstructed in the MS ("combined muons"), or by stand-alone tracks in the MS. They must satisfy impact-parameter requirements: $|d_0|/\sigma(d_0) < 3.0$ and $|z_0 \sin(\theta)| < 0.5$ mm. Muons are required to pass *Tight* or *HighPT* identification requirements [26] based on quality requirements applied to the ID and MS tracks. The *HighPT* selection criteria are applied only for muons with $p_T > 300$ GeV. They must also be isolated: the p_T sum within a variable-radius cone in the ID system around the muon has to be smaller than 0.06 times the muon transverse momentum. The maximum cone size is $\Delta R = 0.3$, shrinking for larger muon p_T.

Electron and muon candidates are required to have a minimum p_T of 7 GeV and to lie within $|\eta| < 2.5$ for muons and $|\eta| < 2.47$ for electrons.

The missing transverse momentum $\vec{E}_T^{\text{miss}}$ is calculated as the negative vectorial sum of the transverse momenta of calibrated electrons, muons, and small-R jets. In addition, a "soft term" is added to take into account energy deposits due to the underlying event and other sources of soft radiation. Similarly, the soft term is computed as the negative vectorial sum of missing transverse momenta of all ID tracks from the primary vertex not associated to any other physics object [86, 87]. The magnitude of $\vec{E}_T^{\text{miss}}$ is defined to be the missing transverse energy, E_T^{miss}.

As leptons and jets are reconstructed and identified independently, this can lead to ambiguous identifications when these objects are spatially close to each other. An overlap removal procedure is therefore applied to uniquely identify these objects.

To improve the mass resolution of the reconstructed Higgs-boson candidates, dedicated energy corrections are applied to both b-tagged small-R and large-R jets to account for semileptonic b-hadron decays. The four-momentum of the closest muon to the jet axis with $p_T > 5$ GeV inside the jet cone is added to the jet four-momentum after removing the energy contribution deposited by the muon in the calorimeter [88, 89]. In this so-called muon-in-jet correction, muons are not required to pass any isolation requirements. For small-R jets including muons, an additional p_T-dependent correction is applied to the jet four-momentum to account for biases in the response of b-jets, improving the resolution of the dijet mass. This correction is determined from simulated SM $VH(H \rightarrow b\bar{b})$ events by calculating the ratio of the p_T of the generator level b-jets from the Higgs boson decay to the p_T of the reconstructed b-tagged jets after the muon-in-jet correction.

5 Analysis strategy and event selection

The search targets the W' decay mode $WH \rightarrow \ell^{\pm} \nu b \bar{b}$ and requires an electron or muon to be reconstructed, the presence of E_T^{miss}, and one or two b-tagged jets to be reconstructed.

Single-electron triggers that identify isolated electrons with the lowest p_T thresholds of $24 - 26$ GeV are used. To recover efficiency for electrons with $p_T > 60$ GeV, triggers without an isolation requirement are also used. The electron candidate that satisfies the trigger is required to match a reconstructed electron with $p_T > 27$ GeV.

For events containing a muon, E_T^{miss} triggers with thresholds of $70 - 110$ GeV are used for the various data-periods, corresponding to increasing instantaneous luminosity. The E_T^{miss} triggers are more efficient than single-muon triggers for the relatively large momentum of the W boson required in the analysis ($p_{T,W} > 150$ GeV) [16]. The trigger efficiency is larger than 95% and fully efficient for $p_{T,W} > 200$ GeV. Events are required to have a reconstructed muon with $p_T > 27$ GeV.

The Higgs-boson candidate is reconstructed from the four-momenta of its decay products, the b-jets. When the Higgs boson has relatively low p_T, the b-quarks can be reconstructed as two small-R jets ("resolved" category). As the momentum of the Higgs boson increases, the two b-quarks become more collimated and a selection using a single large-R jet becomes more efficient ("merged" category). Higgs-boson candidates with one or two b-tagged jets define the "1 b-tag" or "2 b-tag" categories, respectively.

For the resolved signal region, two or three central small-R jets are required. The dijet system is defined by the leading p_T and next-to-leading p_T small-R b-tagged jets when two or three jets are present in the event. In the case where only one b-tagged jet is present, the dijet pair is defined by the b-tagged jet and the leading p_T small-R jet in the remaining set. Events with more than two b-tagged jets are vetoed. Moreover, the four-momentum of the dijet system is scaled by 125 GeV/m_{jj}. The leading p_T jet in the pair must have $p_T > 45$ GeV.

For the merged signal region, a large-R jet is required and the jet should have at least one associated b-tagged VR track jet. For the merged selection, only the leading and sub-leading VR track jets associated with the large-R jet are considered and events with more than two b-tags are excluded from the signal selection. Moreover, events with a b-tagged VR track jet that is not ghost-associated to the large-R jet are rejected from the merged event categories. Events which satisfy the selection requirements of both the resolved and merged categories are assigned to the resolved one due to its better dijet mass resolution and lower background contamination.

The momentum of the neutrino in the z-direction, $p_{z,\nu}$, is obtained by imposing a W-boson mass constraint on the lepton-neutrino system. Here, $p_{z,\nu}$ is taken as either the real component of the complex solution or the real solution with the smallest absolute magnitude from the resulting quadratic equation. The transverse mass of the W boson, $m_{T,W}$, is calculated from the lepton transverse momentum and $\vec{E}_T^{\mathrm{miss}}$. The mass of the WH system, m_{WH}, is the invariant mass calculated from the sum of the four-momenta of the lepton, neutrino, and $H(b\bar{b})$ candidate jets.

Selected events are required to have exactly one isolated *LHTight* electron with $E_T > 27$ GeV or one *Tight* muon with $p_T > 27$ GeV (*HighPT* muon for $p_T > 300$ GeV, as described in Section 4). The multijet background is reduced by requiring $E_T^{\mathrm{miss}} > 80$ (40) GeV for electron (muon) events in the resolved category. In the merged category, the requirement is increased to $E_T^{\mathrm{miss}} > 100$ GeV for both electron and muon events. An m_{WH}-dependent cut is placed on $p_{T,W}$ [16]: it is required to be larger

than the maximum value of 150 GeV or $\left[710 - (3.3 \times 10^5)/m_{WH}\right]$ GeV for the resolved category and $\left[394 \times \ln\left(m_{WH}\right) - 2350\right]$ GeV for the merged category, where m_{WH} is in GeV. Finally, the transverse mass of the W-boson candidate is required to be less than 300 GeV.

Control and signal regions are defined in the sideband and central distribution of $m_{jj}(m_J)$ for both 1 and 2 b-tag resolved (merged) categories. For the resolved (merged) category, the control regions are defined as $50 < m_{jj} < 110$ GeV $||$ $140 < m_{jj} < 200$ GeV ($50 < m_J < 75$ GeV $||$ $145 < m_J < 200$ GeV). Meanwhile, the signal regions are the centre of the distribution with $110 < m_{jj} < 140$ GeV and $75 < m_J < 145$ GeV for resolved and merged categories, respectively. To estimate the multijet background, a dedicated control region is defined by inverting the lepton isolation criteria. This is discussed in Section 6. Table 2 summarises all regions used in the final fit.

Table 2: A list of the signal and control regions included in the analysis.

Region	signal regions	control regions
		Resolved
b-tags	1, 2 b-tag	1, 2 b-tag
Mass window	$110 < m_{jj} < 140$ GeV	$50 < m_{jj} < 110$ GeV $||$ $140 < m_{jj} < 200$ GeV
		Merged
b-tags	1, 2 b-tag	1, 2 b-tag
Mass window	$75 < m_J < 145$ GeV	$50 < m_J < 75$ GeV $||$ $145 < m_J < 200$ GeV

Topological and kinematic selections are summarized in Table 3.

Table 3: Topological and kinematic selections for each category as described in the text for the resolved and merged categories. (†) indicates the selection for the muons while the non indexed value is for electrons.

Variable	Resolved	Merged
Number of jets	≥ 2 central small-R jets	≥ 1 large-R jet
		≥ 2 VR track jets (matched to leading large-R jet)
Leading jet p_T [GeV]	> 45	> 250
m_{jj}/m_J [GeV]	110–140	75–145
Leading lepton p_T [GeV]	> 27	> 27
E_T^{miss} [GeV]	> 80 ($40^\dagger$)	> 100
$p_{T,W}$ [GeV]	$> \max\left[150, 710 - (3.3 \times 10^5 \text{ GeV})/m_{WH}\right]$	$> \max\left[150, 394 \cdot \ln(m_{WH}/(1\text{ GeV})) - 2350\right]$
$m_{T,W}$ [GeV]	< 300	

After all selection criteria are applied, the signal acceptance times efficiency is illustrated in Figure 1 as a function of the W' mass. It ranges from $8 - 28\%$. At lower resonance masses, the resolved category is most efficient, while the efficiency of the merged category increases with the mass and dominates for masses above approximately 1.4 TeV.

The analysis sensitivity is significantly improved for high resonance masses beyond the statistical increase of the data set compared to the previous publication [16]. This is due to the improved reconstruction and analysis techniques described in Section 4 and this Section. Taking advantage of more advanced

jet reconstruction techniques of the TCC large-R jets and b-tagging for boosted topologies with the VR track jets yielded the largest impact. Factoring out the statistical gain of the full Run 2 data set, a total improvement of 20% with a steady increase up to 250% is seen ranging from resonance masses around 1.8 to 5 TeV.
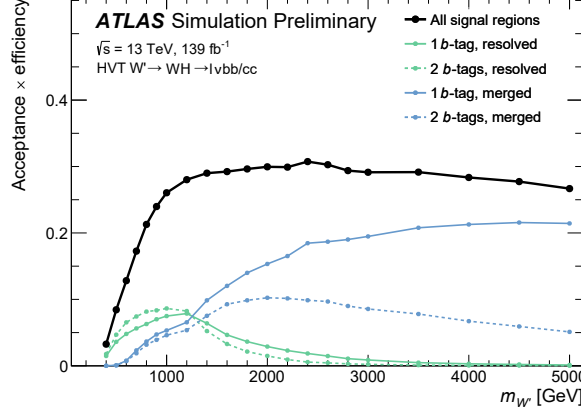

Figure 1: Product of acceptance and efficiency for $pp \to W' \to WH \to \ell\nu bb/cc$ as a function of the resonance mass.

6 Background estimation

The background composition in the signal region is dominated by W+ jets and $t\bar{t}$ with a non-negligible fraction of Z + jets events passing the selections. A small fraction of multijet events is found to pass the tight object selection criteria in the resolved 1-tag category. A data-driven method is used to estimate the multijet background since it is known to be difficult to model in simulation. A template is produced in a dedicated control region enriched with multijet events. Signal leptons from the W bosons are expected to be well-isolated from hadronic activity, while leptons from multijet events are close to jets. The multijet control region is constructed by inverting the lepton isolation requirements described in Section 4. The shape of the m_{WH} template is obtained by subtracting the other sources of background from data, assuming that the other background processes are well modelled in Monte Carlo simulation. An initial normalisation of the template is derived from a two-component fit (multijet and "rest") to data in the m_{jj} side-band control region. An uncertainty on this normalisation is set to 50% for the final fit, and an uncertainty on the shape is derived by observing the shape differences with varied E_T^{miss} cut (± 25%). Further details on the template method can be found in Reference [90].

Simulated event samples of W/Z+jets are split into different flavour components to help improve the grouping of the background components in the final fit as the contribution varies from the 1 b-tag to 2 b-tag categories. In the resolved category, the samples are split according to the generated flavour of the two small-R jets forming the Higgs-boson candidate. In the merged category, they are split according to the generated flavour of the VR track jets associated with the large-R jet. The generated jet flavour is determined by counting generated heavy-flavour hadrons with $p_T > 5$ GeV that are ghost-associated to the reconstructed jet. If a b-hadron is found, the jet is labelled as a b-jet, otherwise if a c-hadron is found the jet is labelled as a c-jet. If neither a b-hadron nor a c-hadron is associated with the reconstructed jet, it is labelled as a light-flavour jet. Based on this association scheme, the W/Z+jets simulated event

samples are split into three components: W/Z+hf (W/Z+bb, W/Z+bc and W/Z+cc), W/Z+hl (W/Z+bl and W/Z+cl) and W/Z+l; in this notation hf, hl and l refer to heavy-flavour jets, heavy- and light-flavour jets, and light-flavour jets, respectively. For W+jets, in the 1 b-tag category W+hl dominates, while for the 2 b-tag region the leading contribution is W+hf. The single-top-quark and $t\bar{t}$ processes are combined into one single background component, which is referred to as top-quark background.

In the statistical analysis described in Section 8 the global normalisations of the dominant backgrounds, top, W+hf, and W+hl backgrounds are determined via fit to data. The m_{jj} (m_J) sidebands are used to constrain the W+jets and top-quark backgrounds in the resolved (merged) category. The results of the fit are discussed in Section 8.

7 Systematic uncertainties

Experimental and modelling uncertainties affect the m_{WH} distribution and enter the final fit as nuisance parameters. The largest experimental systematic uncertainties are associated with the calibration and resolution of the small-R and large-R jet energy and of the large-R jet mass. Further dominant uncertainties are related to the determination of the jet b-tagging efficiency and mis-tagging rate. The uncertainties in the small-R jet energy scale have contributions from limited accuracy in *in situ* calibration studies, from the dependency on the pile-up activity, and from the flavour composition of jets [84, 85]. An additional uncertainty in the energy calibration of b- and c-jets is also used. The uncertainty in the scale and resolution of large-R jet energy and mass is estimated by comparing the ratio of calorimeter-based to track-based measurements in dijet data and simulation [83, 91]. Differences in the b-tagging efficiency measured in data and simulation result in correction factors for b-jets, c-jets and light-flavour jets. Uncertainties on these correction factors are decomposed into uncorrelated components [21, 23, 24]. An additional term is included to extrapolate the measured uncertainties to the high-p_T region of interest. This term is calculated from simulated events by considering variations of the quantities affecting the b-tagging performance such as the impact parameter resolution, percentage of poorly measured tracks, description of the detector material, and track multiplicity per jet [92].

Uncertainties in the reconstruction, identification, isolation and trigger efficiencies of muons [26] and electrons [25] and on their energy scale and resolution have only a small impact on the result. Uncertainties on the E_T^{miss} trigger efficiency are taken into account by following the approach described in Reference [90]. The uncertainties in the energy scale and resolution of the small-R jets and leptons are propagated to the calculation of E_T^{miss}, which also has additional uncertainties from the modelling of the underlying event and momentum scale, momentum resolution and reconstruction efficiency of the tracks used to compute the soft-term [86, 87]. Finally, a global luminosity uncertainty of 1.7% is applied to the normalisation of all non-floating simulated background sources [93, 94].

Modelling uncertainties are derived for both the simulated signal and background processes. They are included in the statistical analysis as shape and normalisation variations. The modelling uncertainties in $t\bar{t}$ are derived as follows: to assess potential differences in the matching between matrix element and parton shower, a comparison is made to a sample where POWHEGBOX 2 is replaced by MADGRAPH 5. The parton shower modelling is assessed by replacing PYTHIA 8 by HERWIG 7 (version 2.7.1). The uncertainty on the modelling of initial-state radiation (ISR) is addressed by changing the renormalisation and factorisation scales by a factor of two in combination with the eigenvariations of the PYTHIA 8 A14 set of tuned parameters. The uncertainty on the modelling of final-state radiation (FSR) is addressed by varying the FSR scale [38].

Parton shower and matrix element variations related to W/Z+jets are accounted for by comparing the nominal samples to alternative ones generated with LO-accurate ME by MadGraph 5 v2.2.2 using NNPDF 3.0 NLO PDF and interfaced to Pythia 8 [37] using the CKKW-L merging procedure [95, 96]. The A14 set of tuned parameters of Pythia 8 is used with the NNPDF 2.3 LO PDF set and decays of bottom and charm hadrons are performed by EvtGen 1.2.0.

For both $t\bar{t}$ and W/Z+jets backgrounds, uncertainties on the PDF are determined by the standard variation of the 101 NNPDF 3.0 NLO replicas, using NNPDF 3.0 NLO PDFs with varied α_s [50] and by comparing with the nominal MMHT2014 NNLO and the CT14 NNLO PDF sets [67].

For the signal processes, uncertainties in the acceptance are derived by replacing the nominal PDF set by the MSTW2008 LO [97] and the CT10 [98] PDF sets, by using the eigenvariations of the Pythia 8 A14 set of tuned parameters [38] and by replacing Pythia 8 by Herwig 7 (version 2.7.1) [99].

For the simulation of signal and major backgrounds, the above-listed theory uncertainties translate into priors for nuisance parameters on the global cross-section and/or acceptance, on the acceptance ratios between different fit regions (signal and control regions, resolved and merged categories), and on the shape of the distribution in the final mass discriminant. For the diboson and SM VH backgrounds only a normalisation uncertainty is assigned, as these processes give only a relatively small contribution to the studied phase space regions. This normalisation uncertainy covers effects on both the cross-section and acceptance [100].

Additional uncertainties arise from residual mismodelling of the transverse momenta of both the large-R jet and the W boson candidate (that is, the $p_{T,\ell} + E_T^{\mathrm{miss}}$ system): the magnitude of both varies depending on m_{WH} and ranges from 1-10%. These are not corrected but the ratios data-to-simulation are used to define systematic uncertainties on the relevant shapes and they are applied to all backgrounds as uncorrelated nuisance parameters.

Due to the exclusive jet multiplicity requirements, variations of the renormalisation and factorisation scales will underestimate uncertainties on perturbative effects [101]. Thus additional uncertainties are assigned to the W+jets background. These uncertainties are evaluated by individually varying the contributions from W+jets events with less than two (more than three) jets at the generator level. In both cases, the contribution to the signal and control regions are varied up/down by 50%. Only the shape uncertainties are retained as the normalisation of W+jets are floating in the final fit. This uncertainty is referred to as "JetBinMigration".

The modelling systematic uncertainties arising discussed above are summarised in Table 4.

8 Results

In order to test the presence of a massive resonance, the m_{WH} templates obtained from the simulated signal and background samples are fit to data using a binned maximum-likelihood approach based on the RooFit/RooStats framework [102–104], where the binning is optimized to maximise the sensitivity of the search while minimising the impact of statistical fluctuations. All signal and control regions shown in Table 2 are included in the fit. The fit is interpreted in two different signal models, as described in Section 1: *Model A*, where the branching fractions to fermions and gauge bosons are comparable, as in some models with an extended gauge symmetry [30]; and *Model B*, where fermionic couplings are suppressed, as in strong dynamical models such as the minimal composite Higgs model [31]. The search focuses on high

Table 4: Relative modeling uncertainties in the normalisation, cross-region extrapolation, and shape of the signal and background processes included in the fits described in the text. An "S" indicates that a shape variation is included for the sources listed, "/" indicates a ratio of the number of events in two regions, and "norm." is the sum of cross-section and acceptance variations. A value of "float" indicates that the parameter is not constrained in the fit. The uncertainty on the normalisation ratios of two regions represents how much the relative normalization of the two regions can vary in the combined fit. A range of values means that the value depends on the lepton channel.

Process	Quantity/source	Value
Signal	acceptance	2-7%
	PS, ISR/FSR, PDF	S
Top	norm.	float
	resolved / merged	18–20%
	m_{jj} SR / m_{jj} CR	2–3%
	PS, ISR/FSR, ME, PDF	S
	$p_{T,W}$ non-closure	S
	Large-R jet p_T non-closure	S
Z+hf	norm.	50%
	resolved / merged	9–18%
	m_{jj} SR / m_{jj} CR	6–20%
	generator, PDF, scale	S
	$p_{T,W}$ non-closure	S
	Large-R jet p_T non-closure	S
Z+hl	norm.	50%
	resolved / merged	12–13%
	m_{jj} SR / m_{jj} CR	5–7%
	generator, PDF, scale	S
	$p_{T,W}$ non-closure	S
	Large-R jet p_T non-closure	S
Z+l	norm.	19%
	resolved / merged	10–29%
	m_{jj} SR / m_{jj} CR	29–99%
	generator, PDF, scale	S
	$p_{T,W}$ non-closure	S
	Large-R jet p_T non-closure	S
W+hf	norm.	float
	resolved / merged	15–22%
	m_{jj} SR / m_{jj} CR	3%
	generator, PDF, scale	S
	$p_{T,W}$ non-closure	S
	Large-R jet p_T non-closure	S
	JetBinMigration	S
W+hl	norm.	float
	resolved / merged	12–13%
	m_{jj} SR / m_{jj} CR	1–2%
	generator, PDF, scale	S
	$p_{T,W}$ non-closure	S
	Large-R jet p_T non-closure	S
	JetBinMigration	S
W+l	norm.	30%
	resolved / merged	20–21%
	m_{jj} SR / m_{jj} CR	2–4%
	generator, PDF, scale	S
	$p_{T,W}$ non-closure	S
	Large-R jet p_T non-closure	S
	JetBinMigration	S
SM VH	norm.	32%
	$p_{T,W}$ non-closure	S
	Large-R jet p_T non-closure	S
Diboson	norm.	50%
	$p_{T,W}$ non-closure	S
	Large-R jet p_T non-closure	S

resonance masses, from 400 GeV up to 5 TeV. The systematic uncertainties described in Section 7 are incorporated in the fit as nuisance parameters with correlations across regions and processes taken into account. The signal cross-section is a free parameter in the fit, as is the global normalisation of the top, W+hf and W+hl backgrounds. Normalisation factors obtained by the fit for top, W+hf and W+hl processes are 0.92 ± 0.04, 1.18 ± 0.14, and 1.27 ± 0.12, respectively.

The expected and observed event yields after the fit are shown in Table 5. The post-fit m_{WH} distributions are shown in Figure 2 for the signal region. Parameter morphing is used to interpolate results for resonance masses that fall between the simulated signal mass points [105].

Table 5: The predicted and observed event yields in the signal regions defined in the text. The quoted uncertainties are the total uncertainties, including both statistical and systematic components. The uncertainties in the individual background predictions are larger than the total background uncertainty due to correlations in the normalisation parameters in the fit.

	Resolved		Merged	
	1 b-tag SR	2 b-tag SR	1 b-tag SR	2 b-tag SR
Top	86911 ±753	18272±111	26215±217	1100±29
Z+hf	80±19	58±12	22±4.5	11±2
Z+hl	561±110	6±1	107±17	1±0
Z+l	117±28	1±0	38±15	0
W+hf	2674±168	1344±76	1120±56	547±28
W+hl	21439±816	126±9	5275±214	29±3
W+l	2706±443	2±1	1240±142	3±1
Diboson	235±30	24±3	370±38	49±5
SM VH	143±16	182±19	31±3	25±2
Multijet	324±81	-	-	-
Total	115190±282	20015±86	34418±123	1765±27
Data	115145	20017	34403	1771

The largest deviation from the SM expectations is found at a resonance mass around 3 TeV and corresponds to a local significance of about 1.1 standard deviations. As no significant excess over the background prediction is observed, upper limits at the 95% confidence level (CL) are set on the production cross-section ($pp \rightarrow W'$) multiplied by the branching fraction BR($W' \rightarrow WH$). The limits are evaluated using a modified frequentist method known as CL_s [106] and the profile-likelihood-ratio test statistic using the asymptotic approximation [107].

The 95% CL upper limits on the production cross-section for $W' \rightarrow WH$ are shown in Figure 3 as a function of the resonance mass. The limits range from 1.3 pb for $m_{W'}$ = 400 GeV to 0.56 fb for $m_{W'}$ = 5 TeV. W' masses below 2.95 TeV are excluded for the HVT benchmark *Model A* with coupling constant $g_V = 1$ [12]. For *Model B* with coupling constant $g_V = 3$, W' masses below 3.15 TeV are excluded. The limits on the $m_{W'}$ = 5 TeV signal hypothesis have also been calculated using pseudo-experiments to validate the asymptotic approximation approach in a phase space region strongly limited by the low amount of recorded data. It was found that both statistical methods agree within 20%. Constraints on the couplings in the g_F vs. g_H plane (defined in Reference [108]) at 95% CL are shown in Figure 4 for three resonance masses of 2, 3 and 4 TeV.[3]

The uncertainties on the data statistics become prevalent for resonance masses above 600 GeV. The dominant systematic uncertainties for low resonance masses (i.e. $m_{W'}$ = 500 GeV) are due to the modelling of the parton shower and FSR of the $t\bar{t}$ background and from mismodelling of the $p_{T,W}$ spectra in W+hf events. At intermediate resonance masses (i.e. $m_{W'}$ = 700 GeV), the major uncertainties come from the mismodelling of the $p_{T,W}$ spectra in $t\bar{t}$ events and the matching of the matrix element and parton shower

---

[3] The coupling constants g_H and g_F are described in Reference [12] as follows: the Higgs coupling $g_H = g_V c_H$ and the universal fermion coupling $g_F = g^2 c_F/g_V$, where g is the SM $SU(2)_L$ gauge coupling.
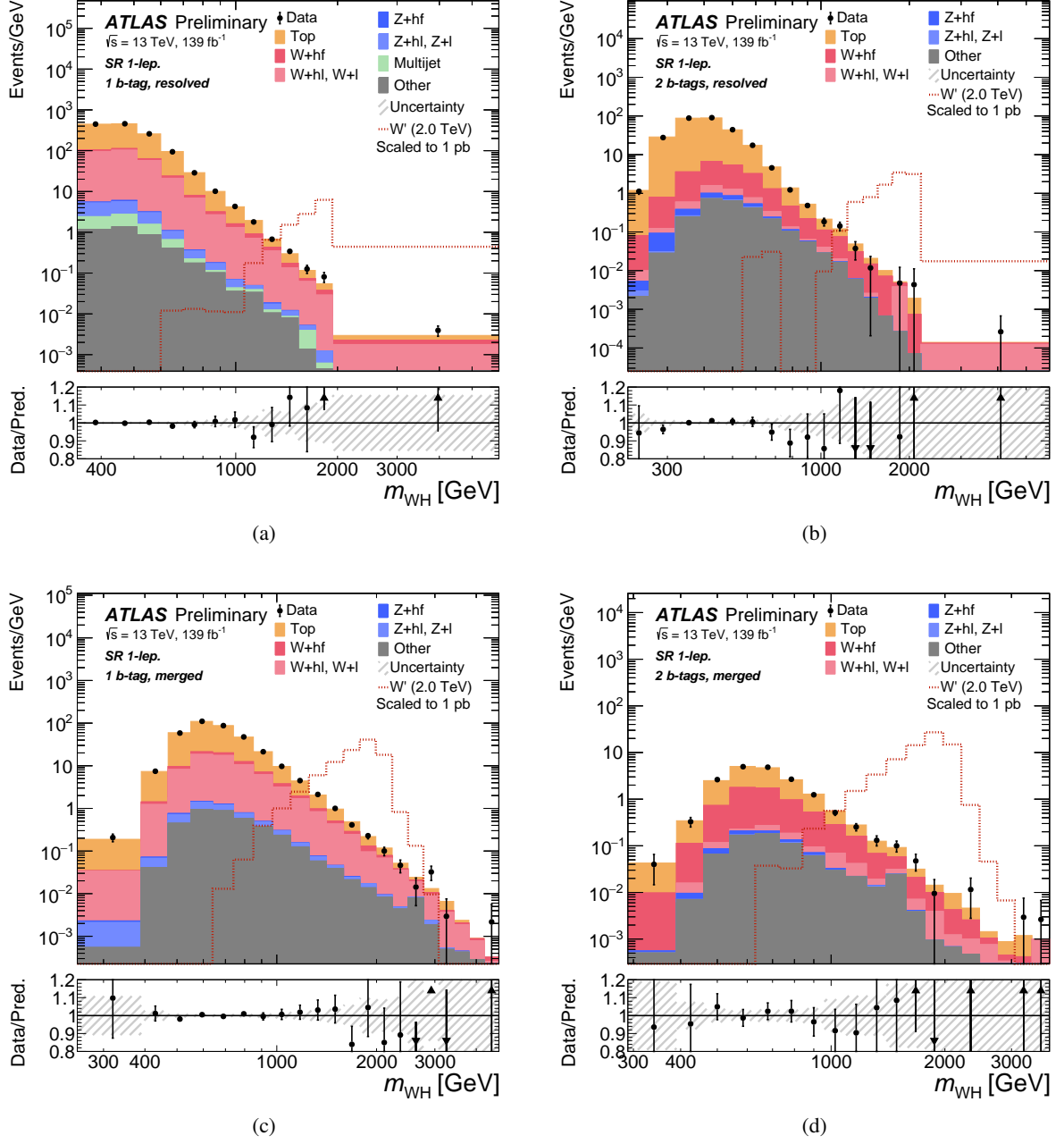
Figure 2: Distributions of m_{WH} for the signal region (a) in the 1-b-tagged resolved category, (b) in the 2-b-tagged resolved category and (c)-(d) accordingly for the same in the merged category. The quantity on the vertical axis is the event yield divided by the bin width in GeV. The background prediction is shown after a background-only maximum-likelihood fit to the data. Small backgrounds (diboson and SM WH) are combined into the grey histogram labeled "Other." The background uncertainty bands include both the statistical and systematic uncertainties after the fit. The lower panels show the ratio of the observed data to the estimated SM background, with arrows indicating bins where the value is out of the scale of the panel. The signal for the benchmark HVT *Model A* with $m_{W'} = 2.0$ TeV is shown as a dashed red line and is normalised to a cross-section of 1 pb.

for $t\bar{t}$ and W+jets background contributions. For higher masses (i.e. $m_{W'} = 2$ TeV) the uncertainty related to the modelling of the large-R jet p_T for $t\bar{t}$ and W+jets events dominates.
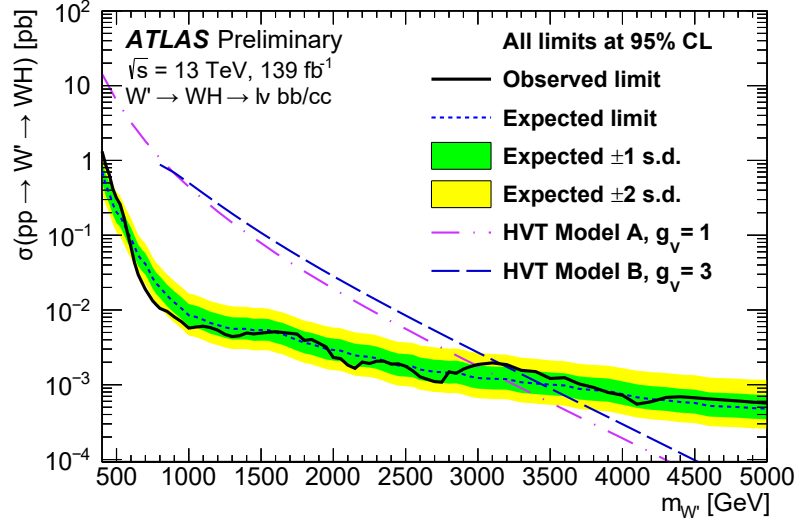
Figure 3: Expected and observed upper limits at 95% CL on the production cross-section for $pp \rightarrow W' \rightarrow WH$. The green (yellow) band indicates ± 1 (± 2) standard deviations of the expected limits. The branching fraction $H \rightarrow b\bar{b}, c\bar{c}$ is assumed to be 0.584. The theory curve for the HVT *Model A* with the resonance coupling $g_V = 1$ is shown as the dotted-dashed purple line and *Model B* with $g_V = 3$ as the dashed dark blue line.
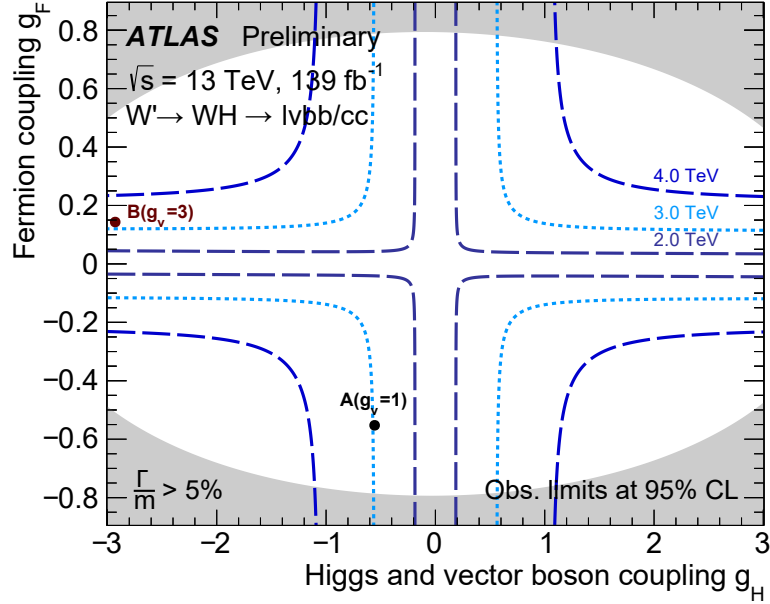
Figure 4: Observed limits on the HVT Model at 95% CL in the g_F vs. g_H plane for W' resonance masses of 2, 3 and 4 TeV. The circles indicate the coupling values for *Models A* and *B* and the grey region corresponds to the area of phase-space where the decay width of the resonance is no longer negligible and the signal m_{WH} shape is no longer expected to be dominated by the experimental resolution.

9 Conclusion

A search for W' bosons that decay into a W boson and a Higgs boson H is performed using 139 fb^{-1} of 13 TeV pp collision data collected with the ATLAS detector at the LHC. The search targets leptonic decays of the W boson ($W \rightarrow \ell\nu$), where $\ell = e$ or μ, and requires b-quark pair decays for the Higgs boson.

No significant excess of events is observed above the SM prediction, and upper limits are set on the production cross-section for $pp \rightarrow W'$ times the branching fraction for $W' \rightarrow WH$. The 95% CL upper limits range from 1.3 pb for $m_{W'} = 400$ GeV to 0.56 fb for $m_{W'} = 5$ TeV. W' masses below 2.95 TeV are excluded for the HVT benchmark *Model A* with coupling constant $g_V = 1$ [12]. For *Model B* with coupling constant $g_V = 3$ [12], W' masses below 3.15 TeV are excluded. The cross-section limits improve on the search results from the analysis on the partial Run 2 data set in ATLAS [17]. The improvements range from about 200% for a resonance mass of 400 GeV to about 350% for a mass of 5 TeV.

References

[1] ATLAS Collaboration, *Observation of a new particle in the search for the Standard Model Higgs boson with the ATLAS detector at the LHC*, Phys. Lett. B **716** (2012) 1, arXiv: 1207.7214 [hep-ex] (cit. on p. 2).

[2] CMS Collaboration, *Observation of a new boson at a mass of 125 GeV with the CMS experiment at the LHC*, Phys. Lett. B **716** (2012) 30, arXiv: 1207.7235 [hep-ex] (cit. on p. 2).

[3] S. Weinberg, *Gauge hierarchies*, Phys. Lett. B **82** (1979) 387 (cit. on p. 2).

[4] M. J. G. Veltman, *The infrared - ultraviolet connection*, Acta Phys. Polon. B **12** (1981) 437 (cit. on p. 2).

[5] C. H. Llewellyn Smith and G. G. Ross, *The real gauge hierarchy problem*, Phys. Lett. B **105** (1981) 38 (cit. on p. 2).

[6] F. Sannino and K. Tuominen, *Orientifold theory dynamics and symmetry breaking*, Phys. Rev. D **71** (2005) 051901, arXiv: 0405209 [hep-ph] (cit. on p. 2).

[7] R. Foadi, M. T. Frandsen, T. A. Ryttov and F. Sannino, *Minimal Walking Technicolor: Set Up for Collider Physics*, Phys. Rev. D **76** (2007) 055005, arXiv: 0706.1696 [hep-ph] (cit. on p. 2).

[8] A. Belyaev et al., *Technicolor walks at the LHC*, Phys. Rev. D **79** (2009) 035006, arXiv: 0809.0793 [hep-ph] (cit. on p. 2).

[9] M. Schmaltz and D. Tucker-Smith, *Little Higgs review*, Ann. Rev. Nucl. Part. Sci. **55** (2005) 229, arXiv: 0502182 [hep-ph] (cit. on p. 2).

[10] M. J. Dugan, H. Georgi and D. B. Kaplan, *Anatomy of a composite Higgs model*, Nucl. Phys. B **254** (1985) 299 (cit. on p. 2).

[11] K. Agashe, R. Contino and A. Pomarol, *The minimal composite Higgs model*, Nucl. Phys. B **719** (2005) 165, arXiv: 0412089 [hep-ph] (cit. on p. 2).

[12] D. Pappadopulo, A. Thamm, R. Torre and A. Wulzer, *Heavy Vector Triplets: Bridging Theory and Data*, JHEP **09** (2014) 060, arXiv: 1402.4431 [hep-ph] (cit. on pp. 2, 13, 16).

[13] J. de Blas, J. M. Lizana and M. Perez-Victoria, *Combining searches of Z' and W' bosons*, JHEP **01** (2013) 166, arXiv: 1211.2229 [hep-ph] (cit. on p. 2).

[14] LHC Higgs Cross Section Working Group, *Handbook of LHC Higgs cross sections: 4. Deciphering the nature of the Higgs sector*, (2016), arXiv: 1610.07922 [hep-ph] (cit. on p. 2).

[15] CMS Collaboration, *Search for beyond the standard model Higgs bosons decaying into a $b\bar{b}$ pair in pp collisions at $\sqrt{s}$ = 13 TeV*, JHEP **08** (2018) 113, arXiv: 1805.12191 [hep-ex] (cit. on p. 2).

[16] ATLAS Collaboration, *Search for heavy resonances decaying to a W or Z boson and a Higgs boson in the $q\bar{q}^{(\prime)}b\bar{b}$ final state in pp collisions at $\sqrt{s}$ = 13 TeV with the ATLAS detector*, Phys. Lett. B **774** (2017) 494, arXiv: 1707.06958 [hep-ex] (cit. on pp. 2, 7, 8).

[17] ATLAS Collaboration, *Search for new resonances decaying to a W or Z boson and a Higgs boson in the $\ell^+\ell^- b\bar{b}$, $\ell \nu b\bar{b}$, and $\nu\bar{\nu}b\bar{b}$ channels with pp collisions at $\sqrt{s}$ = 13 TeV with the ATLAS detector*, Phys. Lett. B **765** (2017) 32, arXiv: 1607.05621 [hep-ex] (cit. on pp. 2, 16).

[18] ATLAS Collaboration, *Search for heavy resonances decaying into a W or Z boson and a Higgs boson in final states with leptons and b-jets in $36\,fb^{-1}$ of $\sqrt{s}$ = 13 TeV pp collisions with the ATLAS detector*, JHEP **03** (2018) 174, arXiv: 1712.06518 [hep-ex] (cit. on p. 2), Erratum: JHEP **11** (2018) 051.

17

[19] ATLAS Collaboration, *Search for resonances decaying into a weak vector boson and a Higgs boson in the fully hadronic final state produced in proton−proton collisions at $\sqrt{s}$ = 13 TeV with the ATLAS detector*, (2020), arXiv: 2007.05293 [hep-ex] (cit. on p. 2).

[20] CMS Collaboration, *Search for heavy resonances that decay into a vector boson and a Higgs boson in hadronic final states at $\sqrt{s}$ = 13 TeV*, Eur. Phys. J. C **77** (2017) 636, arXiv: 1707.01303 [hep-ex] (cit. on p. 2).

[21] ATLAS Collaboration, *ATLAS b-jet identification performance and efficiency measurement with $t\bar{t}$ events in pp collisions at $\sqrt{s}$ = 13 TeV*, Eur. Phys. J. C **79** (2019) 970, arXiv: 1907.05120 [hep-ex] (cit. on pp. 2, 6, 10).

[22] ATLAS Collaboration, *Optimisation and performance studies of the ATLAS b-tagging algorithms for the 2017-18 LHC run*, ATL-PHYS-PUB-2017-013, 2017, URL: https://cds.cern.ch/record/2273281 (cit. on pp. 2, 6).

[23] ATLAS Collaboration, *Measurement of b-tagging efficiency of c-jets in $t\bar{t}$ events using a likelihood approach with the ATLAS detector*, ATLAS-CONF-2018-001, 2018, URL: https://cds.cern.ch/record/2306649 (cit. on pp. 2, 6, 10).

[24] ATLAS Collaboration, *Calibration of light-flavour b-jet mistagging rates using ATLAS proton–proton collision data at $\sqrt{s}$ = 13 TeV*, ATLAS-CONF-2018-006, 2018, URL: https://cds.cern.ch/record/2314418 (cit. on pp. 2, 6, 10).

[25] ATLAS Collaboration, *Electron and photon performance measurements with the ATLAS detector using the 2015-2017 LHC proton-proton collision data*, JINST **14** (2019) P12006, arXiv: 1908.00005 [hep-ex] (cit. on pp. 2, 6, 10).

[26] ATLAS Collaboration, *Muon reconstruction performance of the ATLAS detector in proton–proton collision data at $\sqrt{s}$ = 13 TeV*, Eur. Phys. J. C **76** (2016) 292, arXiv: 1603.05598 [hep-ex] (cit. on pp. 2, 6, 10).

[27] ATLAS Collaboration, *Variable Radius, Exclusive-k_T, and Center-of-Mass Subjet Reconstruction for Higgs($\to b\bar{b}$) Tagging in ATLAS*, tech. rep. ATL-PHYS-PUB-2017-010, CERN, 2017, URL: https://cds.cern.ch/record/2268678 (cit. on pp. 2, 5).

[28] ATLAS Collaboration, *Identification of boosted Higgs bosons decaying into b-quark pairs with the ATLAS detector at 13 TeV*, Eur. Phys. J. C **79** (2019) 836, arXiv: 1906.11005 [hep-ex] (cit. on pp. 2, 5).

[29] ATLAS Collaboration, *Improving jet substructure performance in ATLAS using Track-CaloClusters*, ATL-PHYS-PUB-2017-015, 2017, URL: https://cds.cern.ch/record/2275636 (cit. on pp. 2, 5).

[30] V. D. Barger, W.-Y. Keung and E. Ma, *A gauge model with light W and Z bosons*, Phys. Rev. D **22** (1980) 727 (cit. on pp. 2, 11).

[31] R. Contino, D. Marzocca, D. Pappadopulo and R. Rattazzi, *On the effect of resonances in composite Higgs phenomenology*, JHEP **10** (2011) 081, arXiv: 1109.1570 [hep-ph] (cit. on pp. 2, 11).

[32] ATLAS Collaboration, *The ATLAS Experiment at the CERN Large Hadron Collider*, JINST **3** (2008) S08003 (cit. on p. 3).

[33] ATLAS Collaboration, *ATLAS Insertable B-Layer Technical Design Report Addendum*, tech. rep. CERN-LHCC-2012-009. ATLAS-TDR-19-ADD-1, Addendum to CERN-LHCC-2010-013, ATLAS-TDR-019, 2012, URL: https://cds.cern.ch/record/1451888 (cit. on p. 3).

18

[34] ATLAS Collaboration, *Performance of the ATLAS Trigger System in 2015*, Eur. Phys. J. C **77** (2017) 317, arXiv: 1611.09661 [hep-ex] (cit. on p. 3).

[35] ATLAS Collaboration, *Luminosity determination in pp collisions at $\sqrt{s} = 8$ TeV using the ATLAS detector at the LHC*, Eur. Phys. J. C **76** (2016) 653, arXiv: 1608.03953 [hep-ex] (cit. on p. 3).

[36] J. Alwall et al., *The automated computation of tree-level and next-to-leading order differential cross sections, and their matching to parton shower simulations*, JHEP **07** (2014) 079, arXiv: 1405.0301 [hep-ph] (cit. on p. 3).

[37] T. Sjöstrand, S. Mrenna and P. Skands, *A brief introduction to PYTHIA 8.1*, Comput. Phys. Commun. **178** (2008) 852, arXiv: 0710.3820 [hep-ph] (cit. on pp. 3, 11).

[38] ATLAS Collaboration, *ATLAS Pythia 8 tunes to 7 TeV data*, ATL-PHYS-PUB-2014-021, 2014, URL: https://cds.cern.ch/record/1966419 (cit. on pp. 3, 10, 11).

[39] R. D. Ball et al., *Impact of heavy quark masses on parton distributions and LHC phenomenology*, Nucl. Phys. B **849** (2011) 296, arXiv: 1101.1300 [hep-ph] (cit. on p. 3).

[40] E. Bothmann et al., *Event Generation with Sherpa 2.2*, SciPost Phys. **7** (2019) 034, arXiv: 1905.09127 [hep-ph] (cit. on p. 3).

[41] T. Gleisberg and S. Höche, *Comix, a new matrix element generator*, JHEP **12** (2008) 039, arXiv: 0808.3674 [hep-ph] (cit. on p. 3).

[42] F. Buccioni et al., *OpenLoops 2*, Eur. Phys. J. C **79** (2019) 866, arXiv: 1907.13071 [hep-ph] (cit. on p. 3).

[43] F. Cascioli, P. Maierhöfer, and S. Pozzorini, *Scattering Amplitudes with Open Loops*, Phys. Rev. Lett. **108** (2012) 111601, arXiv: 1111.5206 [hep-ph] (cit. on p. 3).

[44] A. Denner, S. Dittmaier and L. Hofer, *Collier: A fortran-based complex one-loop library in extended regularizations*, Comput. Phys. Commun. **212** (2017) 220, arXiv: 1604.06792 [hep-ph] (cit. on p. 3).

[45] S. Schumann and F. Krauss, *A Parton shower algorithm based on Catani-Seymour dipole factorisation*, JHEP **03** (2008) 038, arXiv: 0709.1027 [hep-ph] (cit. on p. 3).

[46] S. Höche, F. Krauss, M. Schönherr and F. Siegert, *A critical appraisal of NLO+PS matching methods*, JHEP **09** (2012) 049, arXiv: 1111.1220 [hep-ph] (cit. on p. 3).

[47] F Siegert et al., *QCD matrix elements + parton showers: The NLO case*, JHEP **04** (2013) 027, arXiv: 1207.5030 [hep-ph] (cit. on p. 3).

[48] S. Catani, F. Krauss, R. Kuhn and B. R. Webber, *QCD Matrix Elements + Parton Showers*, JHEP **11** (2001) 063, arXiv: hep-ph/0109231 (cit. on p. 3).

[49] S. Höche, F. Krauss, S. Schumann and F. Siegert, *QCD matrix elements and truncated showers*, JHEP **05** (2009) 053, arXiv: 0903.1219 [hep-ph] (cit. on p. 3).

[50] NNPDF Collaboration: R. D. Ball et al., *Parton distributions for the LHC run 2*, JHEP **04** (2015) 040, arXiv: 1410.8849 [hep-ph] (cit. on pp. 3, 11).

[51] C. Anastasiou, L. J. Dixon, K. Melnikov and F. Petriello, *High precision QCD at hadron colliders: Electroweak gauge boson rapidity distributions at NNLO*, Phys. Rev. D **69** (2004) 094008, arXiv: hep-ph/0312266 (cit. on p. 3).

[52] S. Frixione, P. Nason and G. Ridolfi, *A positive-weight next-to-leading-order Monte Carlo for heavy flavour hadroproduction*, JHEP **09** (2007) 126, arXiv: 0707.3088 [hep-ph] (cit. on p. 4).

[53] P. Nason, *A new method for combining NLO QCD with shower Monte Carlo algorithms*, JHEP **11** (2004) 040, arXiv: hep-ph/0409146 (cit. on p. 4).

[54] S. Frixione, P. Nason and C. Oleari, *Matching NLO QCD computations with Parton Shower simulations: the POWHEG method*, JHEP **11** (2007) 070, arXiv: 0709.2092 [hep-ph] (cit. on p. 4).

[55] S. Alioli, P. Nason, C. Oleari and E. Re, *A general framework for implementing NLO calculations in shower Monte Carlo programs: the POWHEG BOX*, JHEP **06** (2010) 043, arXiv: 1002.2581 [hep-ph] (cit. on p. 4).

[56] ATLAS Collaboration, *Studies on top-quark Monte Carlo modelling for Top2016*, ATL-PHYS-PUB-2016-020, 2016, URL: https://cds.cern.ch/record/2216168 (cit. on p. 4).

[57] T. Sjöstrand et al., *An introduction to PYTHIA 8.2*, Comput. Phys. Commun. **191** (2015) 159, arXiv: 1410.3012 [hep-ph] (cit. on p. 4).

[58] M. Beneke, P. Falgari, S. Klein and C. Schwinn, *Hadronic top-quark pair production with NNLL threshold resummation*, Nucl. Phys. B **855** (2012) 695, arXiv: 1109.1536 [hep-ph] (cit. on p. 4).

[59] M. Cacciari, M. Czakon, M. Mangano, A. Mitov and P. Nason, *Top-pair production at hadron colliders with next-to-next-to-leading logarithmic soft-gluon resummation*, Phys. Lett. B **710** (2012) 612, arXiv: 1111.5869 [hep-ph] (cit. on p. 4).

[60] P. Bärnreuther, M. Czakon and A. Mitov, *Percent level precision physics at the Tevatron: First genuine NNLO QCD corrections to $q\bar{q} \rightarrow t\bar{t} + X$*, Phys. Rev. Lett. **109** (2012) 132001, arXiv: 1204.5201 [hep-ph] (cit. on p. 4).

[61] M. Czakon and A. Mitov, *NNLO corrections to top-pair production at hadron colliders: the all-fermionic scattering channels*, JHEP **12** (2012) 054, arXiv: 1207.0236 [hep-ph] (cit. on p. 4).

[62] M. Czakon and A. Mitov, *NNLO corrections to top pair production at hadron colliders: the quark-gluon reaction*, JHEP **01** (2013) 080, arXiv: 1210.6832 [hep-ph] (cit. on p. 4).

[63] M. Czakon, P. Fiedler and A. Mitov, *Total top-quark-pair-production cross section at hadron colliders through $O(\alpha_S^4)$*, Phys. Rev. Lett. **110** (2013) 252004, arXiv: 1303.6254 [hep-ph] (cit. on p. 4).

[64] M. Czakon and A. Mitov, *Top++: A Program for the Calculation of the Top-Pair Cross-Section at Hadron Colliders*, Comput. Phys. Commun. **185** (2014) 2930, arXiv: 1112.5675 [hep-ph] (cit. on p. 4).

[65] S. Frixione, E. Laenen, P. Motylinski, B. R. Webber and C. D. White, *Single-top hadroproduction in association with a W boson*, JHEP **07** (2008) 029, arXiv: 0805.3067 [hep-ph] (cit. on p. 4).

[66] ATLAS Collaboration, *Multi-Boson Simulation for 13 TeV ATLAS Analyses*, ATL-PHYS-PUB-2017-005, 2017, URL: https://cds.cern.ch/record/2261933 (cit. on p. 4).

[67] J. Butterworth et al., *PDF4LHC recommendations for LHC run 2*, J. Phys. G **43** (2016) 023001, arXiv: 1510.03865 [hep-ph] (cit. on pp. 4, 11).

[68] ATLAS Collaboration, *Measurement of the Z/γ^* boson transverse momentum distribution in pp collisions at $\sqrt{s} = 7$ TeV with the ATLAS detector*, JHEP **09** (2014) 145, arXiv: 1406.3660 [hep-ex] (cit. on p. 4).

[69] R. V. Harlander, A. Kulesza, V. Theeuwes and T. Zirke, *Soft gluon resummation for gluon-induced Higgs Strahlung*, JHEP **11** (2014) 082, arXiv: 1410.0217 [hep-ph] (cit. on p. 4).

[70] ATLAS Collaboration, *The Pythia 8 A3 tune description of ATLAS minimum bias and inelastic measurements incorporating the Donnachie–Landshoff diffractive model*, ATL-PHYS-PUB-2016-017, 2016, URL: https://cds.cern.ch/record/2206965 (cit. on p. 5).

[71] D. J. Lange, *The EvtGen particle decay simulation package*, Nucl. Instrum. Meth. A **462** (2001) 152 (cit. on p. 5).

[72] ATLAS Collaboration, *The ATLAS Simulation Infrastructure*, Eur. Phys. J. C **70** (2010) 823, arXiv: 1005.4568 [physics.ins-det] (cit. on p. 5).

[73] GEANT4 Collaboration, *GEANT4: A Simulation toolkit*, Nucl. Instrum. Meth. A **506** (2003) 250 (cit. on p. 5).

[74] ATLAS Collaboration, *Performance of primary vertex reconstruction in proton-proton collisions at $\sqrt{s}$ =7 TeV in the ATLAS experiment*, tech. rep. ATLAS-CONF-2010-069, CERN, 2010, URL: https://cds.cern.ch/record/1281344 (cit. on p. 5).

[75] M. Cacciari, G. P. Salam and G. Soyez, *The anti-k_t jet clustering algorithm*, JHEP **04** (2008) 063, arXiv: 0802.1189 [hep-ph] (cit. on p. 5).

[76] M. Cacciari, G. P. Salam and G. Soyez, *FastJet User Manual*, Eur. Phys. J. C **72** (2012) 1896, arXiv: 1111.6097 [hep-ph] (cit. on p. 5).

[77] ATLAS Collaboration, *Topological cell clustering in the ATLAS calorimeters and its performance in LHC Run 1*, Eur. Phys. J. C **77** (2017) 490, arXiv: 1603.02934 [hep-ex] (cit. on p. 5).

[78] W. Lampl et al., *Calorimeter Clustering Algorithms: Description and Performance*, ATL-LARG-PUB-2008-002, 2008, URL: https://cds.cern.ch/record/1099735 (cit. on p. 5).

[79] ATLAS Collaboration, *Performance of pile-up mitigation techniques for jets in pp collisions at $\sqrt{s}$ = 8 TeV using the ATLAS detector*, Eur. Phys. J. C **76** (2016) 581, arXiv: 1510.03823 [hep-ex] (cit. on p. 5).

[80] D. Krohn, J. Thaler and L.-T. Wang, *Jet trimming*, JHEP **02** (2010) 084, arXiv: 0912.1342 [hep-ph] (cit. on p. 5).

[81] S. Catani, Y. L. Dokshitzer, M. H. Seymour and B. R. Webber, *Longitudinally invariant $k_{\perp}$ clustering algorithms for hadron hadron collisions*, Nucl. Phys. B **406** (1993) 187 (cit. on p. 5).

[82] S. D. Ellis and D. E. Soper, *Successive combination jet algorithm for hadron collisions*, Phys. Rev. D **48** (1993) 3160, arXiv: hep-ph/9305266 (cit. on p. 5).

[83] ATLAS Collaboration, *Identification of Boosted, Hadronically-Decaying W and Z Bosons in $\sqrt{s}$ = 13 TeV Monte Carlo Simulations for ATLAS*, ATL-PHYS-PUB-2015-033, 2015, URL: https://cds.cern.ch/record/2041461 (cit. on pp. 5, 10).

[84] ATLAS Collaboration, *Jet energy scale measurements and their systematic uncertainties in proton–proton collisions at $\sqrt{s}$ = 13 TeV with the ATLAS detector*, Phys. Rev. D **96** (2017) 072002, arXiv: 1703.09665 [hep-ex] (cit. on pp. 5, 10).

[85] ATLAS Collaboration, *Jet energy resolution in proton–proton collisions at $\sqrt{s}$ = 7 TeV recorded in 2010 with the ATLAS detector*, Eur. Phys. J. C **73** (2013) 2306, arXiv: 1210.6210 [hep-ex] (cit. on pp. 5, 10).

[86] ATLAS Collaboration, *Performance of missing transverse momentum reconstruction with the ATLAS detector using proton–proton collisions at $\sqrt{s}$ = 13 TeV*, Eur. Phys. J. C **78** (2018) 903, arXiv: 1802.08168 [hep-ex] (cit. on pp. 6, 10).

[87] ATLAS Collaboration, E_T^{miss} *performance in the ATLAS detector using 2015–2016 LHC pp collisions*, ATLAS-CONF-2018-023, 2018, URL: https://cds.cern.ch/record/2625233 (cit. on pp. 6, 10).

[88] ATLAS Collaboration, *Measurements of WH and ZH production in the* $H \rightarrow b\bar{b}$ *decay channel in pp collisions at* 13 *TeV with the ATLAS detector*, Eur. Phys. J. C **81** (2021) 178, arXiv: 2007.02873 [hep-ex] (cit. on p. 6).

[89] ATLAS Collaboration, *Search for heavy resonances decaying into a W or Z boson and a Higgs boson in final states with leptons and b-jets in 36 fb^{-1} of* $\sqrt{s}$ = 13 *TeV pp collisions with the ATLAS detector*, JHEP **03** (2018) 174, [Erratum: JHEP 11, 051 (2018)], arXiv: 1712.06518 [hep-ex] (cit. on p. 6).

[90] ATLAS Collaboration, *Observation of* $H \rightarrow b\bar{b}$ *decays and VH production with the ATLAS detector*, Phys. Lett. B **786** (2018) 59, arXiv: 1808.08238 [hep-ex] (cit. on pp. 9, 10).

[91] ATLAS Collaboration, *Jet mass reconstruction with the ATLAS Detector in early Run 2 data*, ATLAS-CONF-2016-035, 2016, URL: https://cds.cern.ch/record/2200211 (cit. on p. 10).

[92] *Simulation-based extrapolation of b-tagging calibrations towards high transverse momenta in the ATLAS experiment*, tech. rep., All figures including auxiliary figures are available at https://atlas.web.cern.ch/Atlas/GROUPS/PHYSICS/PUBNOTES/ATL-PHYS-PUB-2021-003: CERN, 2021, URL: https://cds.cern.ch/record/2753444 (cit. on p. 10).

[93] ATLAS Collaboration, *Luminosity determination in pp collisions at* $\sqrt{s}$ = 13 *TeV using the ATLAS detector at the LHC*, tech. rep. ATLAS-CONF-2019-021, CERN, 2019, URL: https://cds.cern.ch/record/2677054 (cit. on p. 10).

[94] G. Avoni et al., *The new LUCID-2 detector for luminosity measurement and monitoring in ATLAS*, JINST **13** (2018) P07017 (cit. on p. 10).

[95] L. Lönnblad, *Correcting the Colour-Dipole Cascade Model with Fixed Order Matrix Elements*, JHEP **05** (2002) 046, arXiv: hep-ph/0112284 (cit. on p. 11).

[96] L. Lönnblad and S. Prestel, *Matching tree-level matrix elements with interleaved showers*, JHEP **03** (2012) 019, arXiv: 1109.4829 [hep-ph] (cit. on p. 11).

[97] A. D. Martin, W. J. Stirling, R. S. Thorne and G. Watt, *Parton distributions for the LHC*, Eur. Phys. J. C **63** (2009) 189, arXiv: 0901.0002 [hep-ph] (cit. on p. 11).

[98] J. Gao et al., *CT10 next-to-next-to-leading order global analysis of QCD*, Phys. Rev. D **89** (2014) 033009, arXiv: 1302.6246 [hep-ph] (cit. on p. 11).

[99] M. Bähr et al., *Herwig++ physics and manual*, Eur. Phys. J. C **58** (2008) 639 (cit. on p. 11).

[100] J. M. Campbell and R. Ellis, *MCFM for the Tevatron and the LHC*, Nucl. Phys. Proc. Suppl. (2010) 205, arXiv: 1007.3492 [hep-ph] (cit. on p. 11).

[101] I. W. Stewart and F. J. Tackmann, *Theory uncertainties for Higgs mass and other searches using jet bins*, Phys. Rev. D **85** (3 2012) 034011 (cit. on p. 11).

[102] L. Moneta et al., *The RooStats project*, 2010, arXiv: 1009.1003 [hep-ph] (cit. on p. 11).

[103] W. Verkerke and D. Kirkby, *The RooFit toolkit for data modeling*, 2003, arXiv: physics/0306116 [physics.data-an] (cit. on p. 11).

[104] M. Baak et al., *HistFitter software framework for statistical data analysis*, Eur. Phys. J. C **75** (2015) 153, arXiv: 1410.1280 [hep-ex] (cit. on p. 11).

[105] M. Baak, S. Gadatsch, R. Harrington and W. Verkerke, *Interpolation between multi-dimensional histograms using a new non-linear moment morphing method*, Nucl. Instrum. Meth. A. **771** (2015) 39 (cit. on p. 12).

[106] A. L. Read, *Presentation of search results: The CL$_s$ technique*, J. Phys. G **28** (2002) 2693 (cit. on p. 13).

[107] G. Cowan, K. Cranmer, E. Gross and O. Vitells, *Asymptotic formulae for likelihood-based tests of new physics*, Eur. Phys. J. C **71** (2011) 1554, arXiv: `1007.1727 [physics.data-an]`, Erratum: Eur. Phys. J. C **73** (2013) 2501 (cit. on p. 13).

[108] ATLAS Collaboration, *Combination of searches for heavy resonances decaying into bosonic and leptonic final states using* 36 fb^{-1} *of proton-proton collision data at* $\sqrt{s}$ = 13 TeV *with the ATLAS detector*, Phys. Rev. D **98** (5 2018) 052008 (cit. on p. 13).